Electronic Research Archive

http://www.aimspress.com/journal/era

ERA, 33(9): 5845–5864.
DOI: 10.3934/era.2025260
Received: 10 April 2025
Revised: 13 September 2025
Accepted: 19 September 2025
Published: 26 September 2025

Research article

Attenuation of backpropagating action potentials in three types of dentate granule cells

Yue Mao[1], **Ming Liu**[1] **and Xiaojuan Sun**[1,2,*]

[1] School of Physical Science and Technology, Beijing University of Posts and Telecommunications, Beijing 100876, China

[2] Key Laboratory of Mathematics and Information Networks (Beijing University of Posts and Telecommunications), Ministry of Education, Beijing 100876, China

* **Correspondence:** Email: sunxiaojuan@bupt.edu.cn.

Abstract: Backpropagating action potentials (bpAPs) are retrograde electrical signals crucial for modulating synaptic plasticity. They play a pivotal role in regulating neuronal computation and memory formation. In dentate gyrus granule cells, which are key neuronal populations responsible for pattern separation and memory storage, bpAPs-mediated signaling is particularly important for integrating synaptic inputs and fine-tuning network activity. However, this neuronal population has marked structural and functional heterogeneity, including regular granule cells (GCs), semilunar granule cells (SGCs), and hilar ectopic granule cells (HEGCs). The influence of the distinct biophysical properties of these GC subtypes on backpropagation dynamics such as attenuation amplitude, velocity, and spatial spread remains unclear. Here, we utilized multi-compartment models of three types of GCs to systematically investigate the backpropagation efficiency across three metrics: attenuation amplitude, attenuation rate, and propagation distance. We found that higher dendritic K^+ channel density drove strong attenuation of bpAPs in SGCs (highest rate, shortest propagation), whereas higher dendritic Na^+ channel density in HEGCs minimized attenuation. Dendritic branching patterns modulated attenuation amplitude secondarily, while passive axial resistance had negligible effects. These findings establish dendritic active properties rather than morphology as the dominant regulator of attenuation intensity and reveal how activity regulation in these neuronal subtypes contributes to pattern separation and memory storage.

Keywords: backpropagation; attenuation; granule cell; semilunar granule cell; hilar ectopic granule cell; dentate gyrus; multi-compartment model

1. Introduction

Action potentials propagating in different directions along the dendrites of neurons serve distinct functions [1, 2]. Specifically, backpropagating action potentials (bpAPs), which involve the retrograde propagation of action potentials from the soma or axon initial segment to the dendrites, play a critical role in regulating synaptic plasticity associated with learning and memory [3–5]. During backpropagation, attenuation occurs, preventing action potentials triggered by multiple presynaptic inputs from exerting an overly strong influence on the postsynaptic response. This ensures orderly forward propagation of action potentials along dendrites [3, 6]. Moreover, this moderate attenuation allows synaptic inputs to interact at more appropriate intensity upon reaching the dendrites, thereby optimizing information integration efficiency. For example, the attenuation of bpAPs can modulate N-methyl-D-aspartate receptor-mediated Ca^{2+} currents, thereby adjusting synaptic efficacy [1]. Typically, this attenuation is quantified by propagation efficiency, with the two factors being negatively correlated [4].

It is important to highlight that the attenuation of bpAPs serves distinct functions in different types of neurons. In dentate granule cells, Schmidt-Hieber [7] demonstrated that bpAPs exhibit weak attenuation as they propagate to distal dendrites, thereby enhancing dendritic spikes and facilitating coincidence detection. Conversely, in cerebellar Purkinje cells, attenuation decreases significantly during propagation from the soma to distal dendrites due to inefficient backpropagation, resulting in negligible effects on dendritic signal strength [8]. These differences in attenuation of bpAPs can be attributed to the distinct intrinsic properties of neurons [9]. Specifically, passive properties (membrane resistance, axial resistance, membrane capacitance), active properties (density distribution of Na^+ and K^+ channels), and dendritic morphology (branching patterns, geometric ratio) all influence backpropagation efficiency. Moreover, various factors affect different aspects of backpropagation efficiency, including attenuation intensity, propagation distance, and velocity. For instance, in CA1 pyramidal neurons, Herreras [10] found that dendritic membrane resistance is negatively correlated with the amplitude of bpAPs. Additionally, Turner [11] observed that sodium currents can induce axonal burst firing and propagate over long distances to the dendrites of most interneurons. Furthermore, unique dendritic morphology contributes to relatively high efficiency of bpAPs in dopamine neurons [2]. However, an increasing number of dendritic branch orders can reduce velocity of bpAPs [12].

Within the dentate gyrus (DG), granule cells heterogeneity encompasses three principal subtypes: regular granule cells (GCs), semilunar granule cells (SGCs), and hilar ectopic granule cells (HEGCs). While classical GCs in the granule cell layer mediate pattern separation through sparse coding mechanisms [13, 14], SGCs demonstrate stable dendritic excitability that may optimize input discrimination [15]. In contrast, HEGCs—aberrantly localized GCs that emerge following epileptic seizures—disrupt normal circuit dynamics and impair memory functions [16]. Our previous investigations revealed subtype-specific differences in dendritic integration [17], yet the characteristics of bpAPs distinguishing these subtypes of GCs remain uncharacterized, despite their crucial role in regulating synaptic plasticity [18, 19].

Recent investigations into the attenuation of bpAPs in GCs have been strongly motivated by their critical roles in neural circuit operations [20]. These specialized neurons, distributed across multiple brain regions, including the hippocampus and cerebellum, serve as fundamental units for cognitive

processing. However, traditional neural network paradigms, particularly integrate-and-fire models, frequently fail to capture intricate dendritic computations due to their oversimplification of signal propagation dynamics [21]. Contemporary research has uncovered sophisticated biophysical mechanisms within GC dendrites that enable coordinated signal integration and propagation, supporting dentate gyrus-specific neuronal coding and memory consolidation processes [22].

Notably, emerging evidence highlights functional divergence among subtypes of GCs. SGCs enhance pattern separation efficiency through optimized dendritic signal processing, offering new perspectives on information transmission mechanisms [15, 23]. Conversely, HEGCs and their pathological counterparts that emerge during epileptogenesis induce maladaptive plasticity via aberrant structural reorganization. This ultimately impairs pattern separation and memory storage capabilities. The subtype-specific functional profiles highlight the critical need for detailed investigations into their biophysical determinants.

Through this study, we aim to achieve a more comprehensive understanding of the attenuation of bpAPs in GCs, SGCs, and HEGCs. We will investigate the intricate signaling processes within various neurons and evaluate the significance of diverse factors influencing bpAPs within dendrites. This research will enhance our comprehension of these neurons' roles in brain functions such as information processing, learning, and memory formation. To achieve this, we will employ detailed biophysical multi-compartment models that we have developed to analyze how intrinsic properties—both passive and active—of these neurons affect their bpAPs. Specifically, for passive properties, we will examine parameters such as membrane resistance, axial resistance, and membrane capacitance. For active properties, we will focus on various voltage-gated ion channels, including Na^+ and K^+ channels. Additionally, we will consider morphological characteristics such as dendritic branching patterns and geometric ratios. The insights to be gained from studying bpAPs in three GC subtypes may provide a deeper understanding of their unique roles in pattern separation and other associated functions within the DG.

2. Methods

All simulations were conducted using NEURON 7.8 [24], with identical simulation parameters (time step = 0.1 ms) across Windows 10 and macOS platforms to ensure cross-system consistency.

The models for GCs, SGCs, and HEGCs are built upon our prior research and incorporate both passive and active properties [17]. The passive properties consist of membrane resistance (R_m), axial resistance (R_a), membrane capacitance (C_m), resting membrane potential (V_{rest}), reversal potential (E), and the maximum conductance of leakage currents ($\overline{g}_{\text{leak}}$). The active properties encompass the following voltage-dependent currents: the transient Na^+ current (I_{Na}), the fast and slow delayed rectifier potassium currents ($I_{\text{fK}_{\text{DR}}}$ and $I_{\text{sK}_{\text{DR}}}$), the A-type K^+ current ($I_{\text{K}_{\text{A}}}$), the M-type K^+ current ($I_{\text{K}_{\text{M}}}$), the T-type Ca^{2+} current ($I_{\text{Ca}_{\text{T}}}$), the N-type Ca^{2+} current ($I_{\text{Ca}_{\text{N}}}$), the L-type Ca^{2+} current ($I_{\text{Ca}_{\text{L}}}$), the BK-type Ca^{2+}-dependent K^+ current (I_{BK}), the SK-type Ca^{2+}-dependent K^+ current (I_{SK}), the slow afterhyperpolarizing current (I_{sAHP}), and some unknown currents (I_{UK}). Additionally, an extra V-type potassium current ($I_{\text{K}_{\text{V}}}$), as mentioned by Kim [25], is incorporated into the SGC model. It should be noted that the density of ion channel currents (I_{ion}) varies across different dendritic regions. Based on the dynamic equation of I_{ion}, we are able to adjust the corresponding maximum conductance ($\overline{g}_{\text{ion}}$) to represent the density of ion channels.

Regarding the SGC model, in addition to the aforementioned K_V channels, the distribution density of the BK, SK, Ca_T, Ca_N, and Ca_L channels also differ from those in GCs and HEGCs. More specifically, on the proximal dendrites, the distribution density of these ion channels are significantly smaller than those in the other two types of GCs. Furthermore, among the three, SGCs have the smallest $\overline{g}_{leak}$, while they have the largest membrane capacitance. For HEGCs, their E_{leak} is the smallest among the three types of GCs. Moreover, the density of Ca_T channels distributed on its dendrites is the highest, especially on the middle and distal dendrites, where the distribution density far exceeds that of the other two types of GCs.

Based on the constructed GC, SGC, and HEGC models and their parameter configurations, we further examined whether these models can reliably reflect the discharge characteristics of their corresponding neuronal subtypes. To this end, somatic current injection experiments were performed to test their spike trains, and the simulated results were compared with experimental observations. The models reproduced, to a considerable extent, the distinct firing patterns of each neuronal type, and their electrophysiological properties largely fell within the ranges reported in previous experimental studies. A detailed description of the validation procedures and comparisons with biological recordings can be found in our earlier work [17], which provides additional support for the reliability of the present models.

3. Results

3.1. Attenuation of backpropagating action potential

The backpropagating action potential is generated at the soma and then spreads along the dendritic branches toward the distal end. Due to the unique characteristics of different neurons, during the propagation of action potentials, there are different levels of loss, and the transmitted signals are filtered to varying degrees.

In order to conduct a systematic comparison of the attenuation of bpAPs among GCs, SGCs, and HEGCs, we adopted a standardized protocol, which involved somatic current injection (150 pA, 500 ms) along with simultaneous dendritic action potential recording in each type of granule cell (Figure 1a–c). As illustrated in Figure 1d–f, when currents were injected into the soma, action potentials spread along the dendritic branches. To clearly observe the attenuation of action potentials at different positions on the dendritic branches, we quantified the normalized action potential amplitudes ($V_{normalized} = V_{dendrite}/V_{soma}$) at various dendritic branch locations.

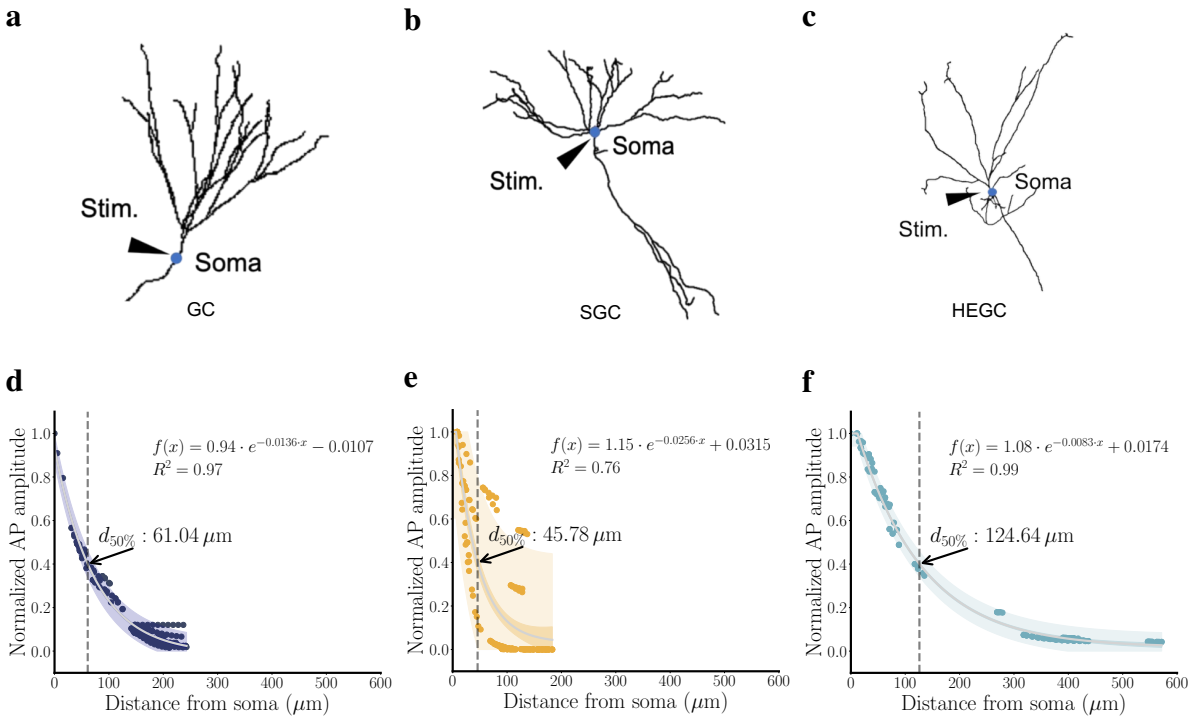

Figure 1. Attenuation of backpropagation in three types of granule cells. a–c) The corresponding neuron morphology of GCs, SGCs, and HEGCs, and the stimulation location of the current injection at the soma (blue dot) of each type of neuron. d–f) Scatter plots depicting the normalized action potential amplitudes across entire dendritic trees for GCs (dark blue dots), SGCs (yellow dots), and HEGCs (light blue dots). Fit curves (light gray lines) were applied to these datasets to demonstrate the attenuation of bpAPs. Y-axis: Normalized action potential amplitude; X-axis: Distance from the soma to the recorded position on the dendrite; $d_{50\%}$: propagation distance; R^2 (coefficients of determination): a metric that evaluates the goodness of fit of the exponential decay function. The light-colored shaded region represents the prediction interval, and the darker shaded region represents the confidence interval.

For a more systematic comparison of attenuation intensity among the three cell types, their respective bpAP datasets were fitted using the exponential decay function $f(x) = ae^{-bx} + c$, as marked in Figure 1d–f. For GCs, the goodness of fit $R^2 = 0.97$, indicating that the fitting function can well fit its attenuation intensity; the 95% confidence intervals of the parameters are relatively narrow ($a \in [0.91, 0.97]$, $b \in [0.0126, 0.0146]$, $c \in [-0.0260, 0.0046]$), and the estimated values of each parameter ($a = 0.94$, $b = 0.0136$, $c = -0.0107$) are stable, verifying the applicability of the fitting function. For HEGCs, the goodness of fit $R^2 = 0.99$, meaning the fitting function has the best fitting degree for its attenuation intensity; the 95% confidence intervals of the parameters are narrow ($a \in [1.07, 1.10]$, $b \in [0.0078, 0.0087]$, $c \in [0.0065, 0.0283]$), and the estimated values of each parameter ($a = 1.08$, $b = 0.0083$, $c = 0.0174$) are highly stable, further supporting the applicability of

the current fitting function. For SGCs, the goodness of fit $R^2 = 0.76$, showing that the fitting function has a relatively poor fitting degree for its datasets; the 95% confidence intervals of the parameters are wider ($a \in [1.01, 1.29]$, $b \in [0.0179, 0.0333]$, $c \in [-0.0392, 0.1021]$), and the fluctuation range of the parameter estimates ($a = 1.15$, $b = 0.0256$, $c = 0.0315$) is slightly larger, but still within the statistically credible range. This relatively lower goodness of fit mainly arises from the morphological characteristics of SGCs, whose dendrites extend at large angles and are spatially dispersed, leading to more scattered data points collected from their dendritic trees. Such dispersion reduces the fitting accuracy to some extent but does not compromise the reliability of the observed overall trend. In summary, this exponential decay function is applicable to the analysis of attenuation intensity for all three types of granule cells. Turning to the parameters of the exponential decay function, a represents the attenuation amplitude, which indicates the magnitude of signal reduction; b determines the attenuation rate, which characterizes the spatial decay speed along the dendrites; and c is responsible for the vertical translation of the function. Apart from using the parameters of the exponential decay function to describe the attenuation intensity, there is also a metric known as the propagation distance ($d_{50\%}$), as mentioned in [26]. It is defined as the distance from the soma at the point where the amplitude of the dendritic action potential decreases to 50% of the somatic action potential amplitude. Larger propagation distances indicate higher signal fidelity with less attenuation.

Nevertheless, a comprehensive evaluation requires a combined analysis of all three metrics. Through exponential curve fitting, we discovered systematic differences in key parameters, as illustrated in Figure 2. The results revealed that with respect to the attenuation amplitude, SGCs had a value of 1.15, which were greater than that of HEGCs (1.08) and GCs (0.94). In terms of the attenuation rate, SGCs were 0.0256, which were higher than those of GCs (0.0136) and HEGCs (0.0083). When they came to the propagation distance, HEGCs were 124.64 μm, which were longer than that of GCs (61.04 μm) and SGCs (45.78 μm).

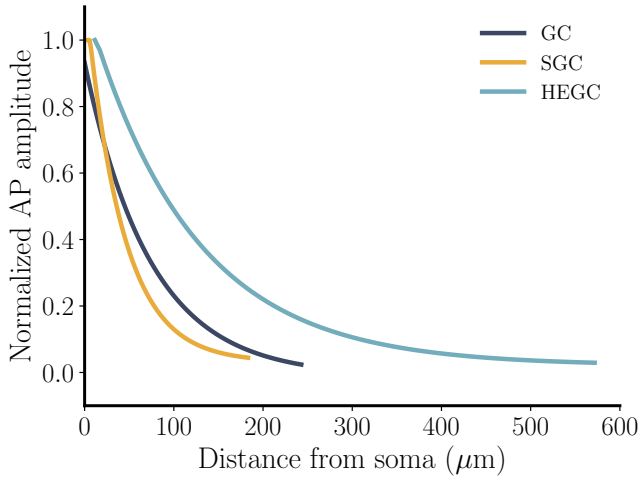

Figure 2. Comparison of attenuation intensity among three types of granule cells. Fit curves for GCs (dark blue line), SGCs (yellow line), and HEGCs (light blue line) illustrate the mean changes in normalized action potential amplitude along the dendrites.

Based on the above results, it can be concluded that SGCs exhibit the strongest attenuation (with

the highest values of a and b, and the shortest $d_{50\%}$). In contrast, HEGCs show the weakest attenuation (having the lowest value of b and the longest $d_{50\%}$), while GCs have intermediate values. Thus, the ranking in terms of attenuation intensity from the strongest to the weakest is SGC > GC > HEGC. Consequently, we can infer that SGCs have the strongest attenuation and low propagation efficiency. On the other hand, the weak attenuation of HEGCs indicate high fidelity for the propagation of dendritic signals, but it also implies that a large amount of redundant information is retained.

3.2. Influence of passive properties on the attenuation of backpropagating action potential

The influence of passive properties on the attenuation of bpAPs was systematically investigated through parametric sensitivity analyses encompassing membrane resistance (R_m), axial resistance (R_a), membrane capacitance (C_m), and leak conductance ($\overline{g}_{\text{leak}}$). These parameters, which collectively govern the cable properties of dendritic arbors, exhibited subtype-specific modulation patterns when varied across physiological ranges.

Specifically, to explore the influence of these passive properties on attenuation intensity across granule cell subtypes, we systematically adjusted R_m, R_a, C_m, and $\overline{g}_{\text{leak}}$ to 3×, 0.5×, 0.3×, and 0.1× of their baseline values, respectively, with the baseline values available in our previous work [17] (Figure 3). While R_m modulation had negligible effects on attenuation intensity in all granule cell types, alterations to C_m and $\overline{g}_{\text{leak}}$ subtly reshaped the fitted curves of GCs and SGCs but left HEGCs largely unaffected. Among these parameters, R_a emerged as the primary determinant of attenuation intensity. To quantify R_a's impact on key metrics (attenuation amplitude, attenuation rate, and propagation distance), we employed the coefficient of variation ($CV = \frac{\sigma}{\mu} \times 100\%$), with σ and μ denoting standard deviation and mean, respectively. Despite R_a manipulations, attenuation amplitude ($CV_{\text{GC, SGC, HEGC}} = 8.372\%, 5.632\%, 2.786\%$; Figure 4a and attenuation rate ($CV_{\text{GC, SGC, HEGC}} = 34.993\%, 44.721\%, 21.287\%$; Figure 4b remained relatively stable across R_a manipulations. As shown in Figure 4c, progressive reduction of R_a from 3-fold to 0.1-fold baseline values revealed differential sensitivity across subtypes, GCs showed a 4-fold increase in propagation distance (37.75 μm → 155.63 μm, $CV = 59.2\%$), whereas SGCs and HEGCs exhibited minimal variation ($CV_{\text{SGC, HEGC}} = 30.628\%, 18.819\%$). From this, we observed that the change in R_a significantly influences the propagation distance.

Comparative analysis of baseline parameters revealed that the relationship between R_a and propagation distance was not regular. While R_a values followed SGC (240 Ω·cm) > HEGC (140 Ω·cm) > GC (130 Ω·cm), propagation distances exhibited the inverse hierarchy HEGC > GC > SGC. This dissociation indicates that R_a significantly influences propagation metrics but does not exclusively determine functional divergence across subtypes.

Consequently, these findings collectively demonstrate that although R_a predominantly affects propagation distance—one of the key determinants of attenuation intensity—it cannot fully account for observed subtype differences. Comprehensive attenuation assessment requires integration of multiple biophysical parameters, with R_a serving as the principal but non-exclusive modulator of dendritic signal propagation.

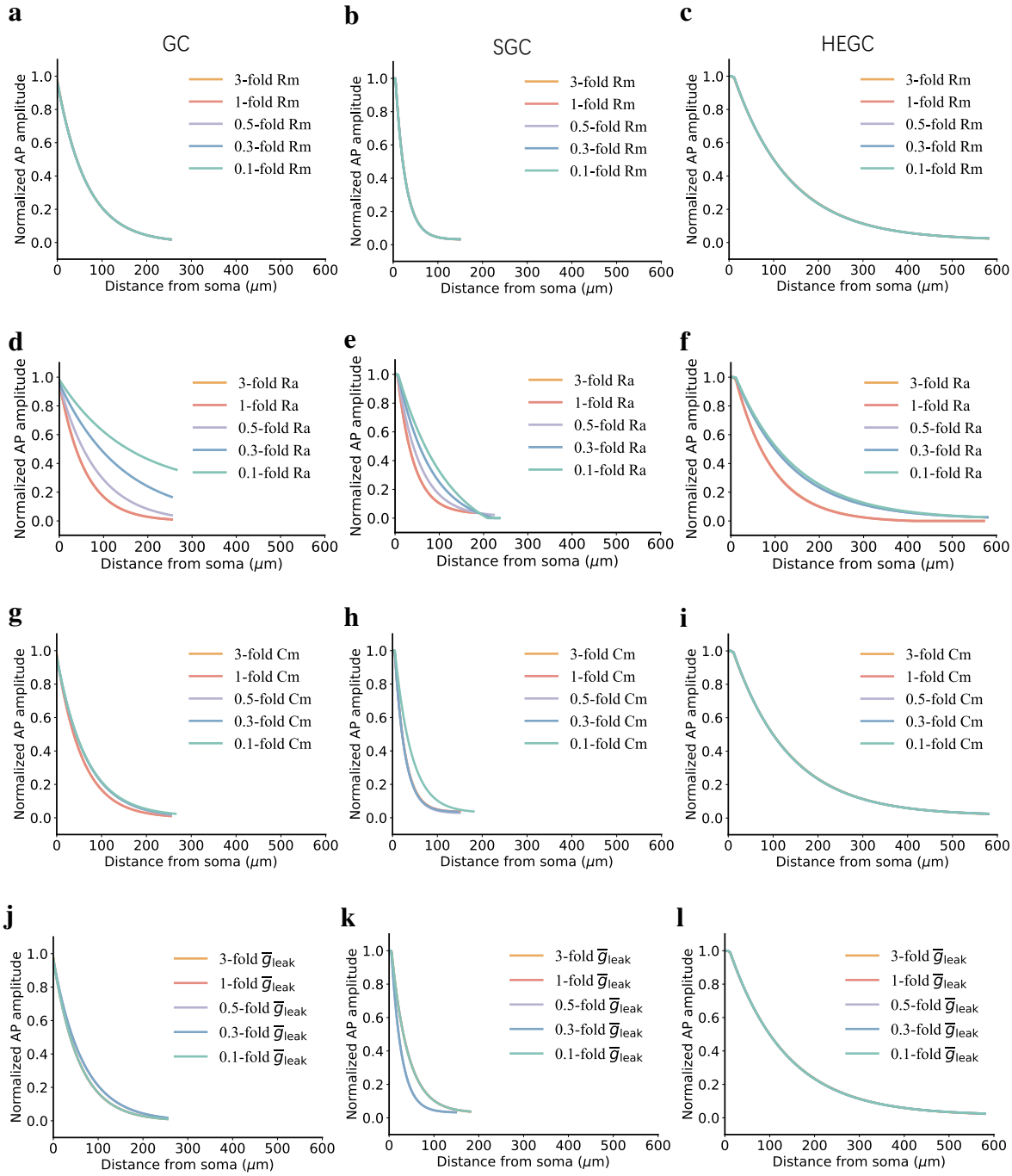

Figure 3. Influence of passive properties on the attenuation of bpAPs. a, d, g, j) For GCs, attenuation intensity, which is manifested as a gradual decrease in normalized action potential amplitude with distance from the soma, persists under the following parameter conditions. The values of R_m, R_a, C_m, and $\overline{g}_{\text{leak}}$ are adjusted to 3-(yellow line), 1-(red line), 0.5-(purple line), 0.3-(blue line), and 0.1-fold(green line) of the original values, respectively. Similarly, the same experimental operations were conducted in b, e, h, k for SGCs and c, f, i, l for HEGCs.

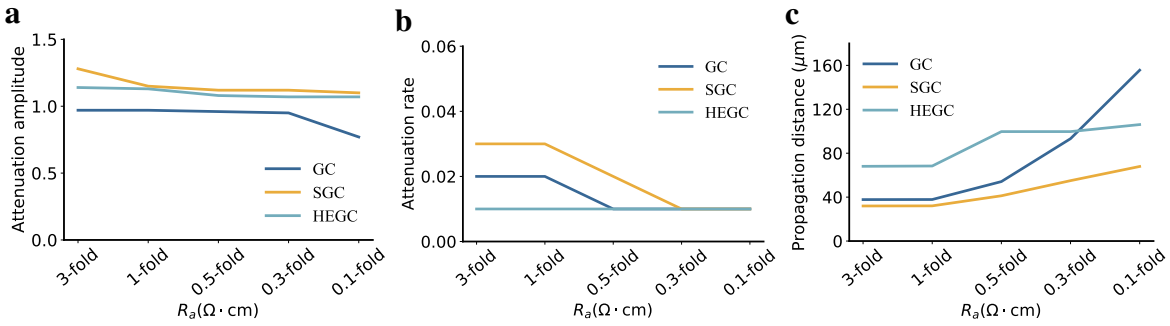

Figure 4. Influence of axial resistance on the attenuation of bpAPs. Quantitative comparison of three types of granule cells in terms of a) attenuation amplitude, b) attenuation rate, and c) propagation distance of axial resistance. GCs: dark blue line; SGCs: yellow line; HEGCs: light blue line.

3.3. Influence of active properties on the attenuation of backpropagating action potential

Our study delved deep into the impact of the density of voltage-gated ion channels on the backpropagation across different neuron types. Previous work by Waters [9] proposed that Na^+ influx in neurons enhances the efficiency of backpropagation along dendrites, whereas Goldberg [27] demonstrated that K^+ channels dampen the backpropagation along dendrites. Specifically, sodium and potassium voltage-gated ion channels were shown to significantly influence the propagation distance of bpAPs [28].

As demonstrated in Figure 5a–c, increasing sodium channel density ($\overline{g}_{\mathrm{Na}}$) significantly altered attenuation intensity. We systematically modulated $\overline{g}_{\mathrm{Na}}$ across a 9-fold range (1× to 9× baseline values) and quantified attenuation effects through three metrics: amplitude, rate, and propagation distance. When $\overline{g}_{\mathrm{Na}}$ was elevated from 1× to 9× baseline values, with the baseline values available in our previous work [17], attenuation rates decreased in GCs (0.016→0.009), SGCs (0.019→0.004), and HEGCs (0.02→0.012) (Figure 5e; $CV_{\mathrm{GC,\,SGC,\,HEGC}} = 18.803\%, 63.943\%, 21.287\%$). Meanwhile, when the conductance was raised to 9-fold of the baseline levels, the propagation distance increases extended by 64.8 μm in HEGCs, 32.7 μ GCs, and 79.49 μm in SGCs (Figure 5f; $CV_{\mathrm{GC,\,SGC,\,HEGC}} = 22.635\%$, 28.377%, 28.898%). Attenuation amplitude remained stable throughout these manipulations (Figure 5d; $CV_{\mathrm{GC,\,SGC,\,HEGC}} = 1.788\%, 11.448\%, 2.004\%$), indicating sodium currents primarily regulated propagation distance and reduced the attenuation rate.

Applying analogous methodology to K^+ channel density, including the proportional simultaneous scaling of the subtype K^+ channels corresponding to each type of granule cell (i.e., $\overline{g}_{\mathrm{K_A}}$, $\overline{g}_{\mathrm{K_M}}$, $\overline{g}_{\mathrm{K_V}}$, $\overline{g}_{f\mathrm{K_{DR}}}$, $\overline{g}_{s\mathrm{K_{DR}}}$, $\overline{g}_{\mathrm{BK}}$, $\overline{g}_{\mathrm{SK}}$), revealed reciprocal effects, with the baseline values of these conductances reported in our previous work [17]. A 9-fold density increase tripled attenuation rates in SGCs (0.026 → 0.054) and halved HEGCs' propagation distances (105.43 μm → 48.51 μm), with minimal amplitude effects (Figure 5g–l; attenuation amplitude, $CV_{\mathrm{GC,\,SGC,\,HEGC}} = 0.811\%, 3.621\%, 4.541\%$; attenuation rate, $CV_{\mathrm{GC,\,SGC,\,HEGC}} = 21.082\%, 23.750\%, 21.287\%$; propagation distance, $CV_{\mathrm{GC,\,SGC,\,HEGC}} = 26.680\%, 24.540\%, 31.242\%$). These results established that potassium channel density potently impedes bpAPs through combined propagation distance and attenuation

rate modulation.

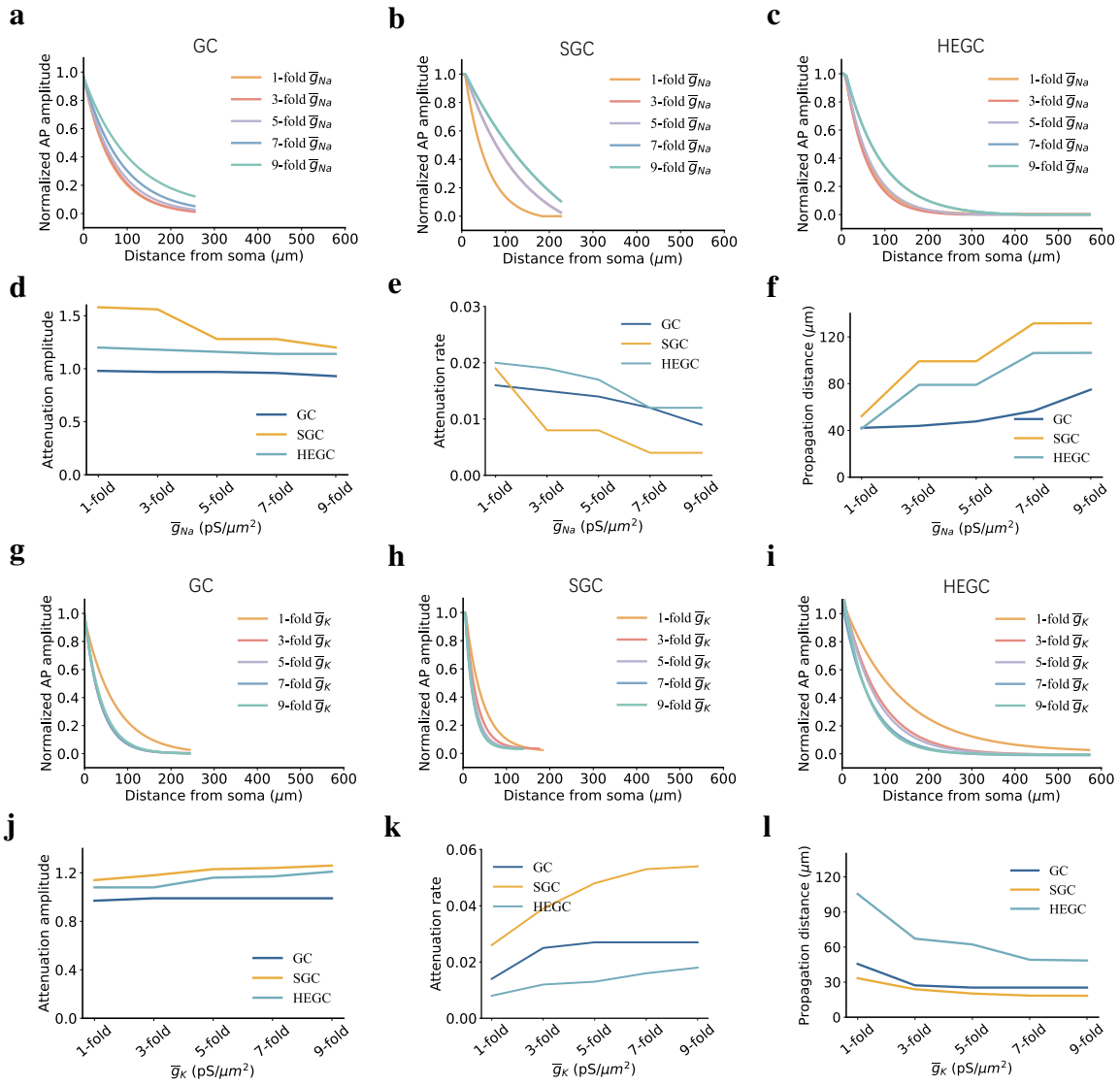

Figure 5. Influence of different Na^+ and K^+ channel distribution densities on the attenuation of bpAPs. For a) GCs, b) SGCs, and c) HEGCs, when $\overline{g}_{\mathrm{Na}}$ in the dendrite increases by odd multiples up to 9-fold of the original, the normalized action potential amplitude varies with the soma distance. As $\overline{g}_{\mathrm{Na}}$ increases, the corresponding d) attenuation amplitude, e) attenuation rate, and f) propagation distance may change. Similarly, for g) GCs, h) SGCs, and i) HEGCs, when $\overline{g}_{\mathrm{K}}$ in the dendrite increases by odd multiples up to 9-fold of the original, the normalized action potential amplitude changes with the soma distance. With the increase of $\overline{g}_{\mathrm{K}}$, the j) attenuation amplitude, k) attenuation rate, and l) propagation distance of GCs, SGCs, and HEGCs are affected, respectively. Line coding: GCs (dark blue), SGCs (yellow), HEGCs (light blue); Conductance multiples: 1-(yellow), 3-(red), 5-(purple), 7-(blue), 9-fold (green).

Previously, we hypothesized that the attenuation intensity of bpAPs is associated with the total density of Na^+ channels and K^+ channels across different types of neurons. To test this hypothesis, we quantified the distribution density of Na^+ and K^+ channels in three types of GCs, focusing specifically on the total values of $\overline{g}_{Na}$ and $\overline{g}_{K}$ in dendrites to observe changes in their distribution density. As shown in Figure 6a, the $\overline{g}_{Na}$ density hierarchy (HEGC > GC > SGC) inversely correlated with our experimental attenuation intensity rank (SGC > GC > HEGC), confirming that elevated Na^+ channel density reduced signal attenuation. Conversely, dendritic $\overline{g}_{K}$ levels (SGC > GC > HEGC, Figure 6b) directly aligned with attenuation intensity, demonstrating potassium channels' pro-attenuation effects.

Therefore, our results indicate a positive correlation between Na^+ channel density and attenuation intensity, while there is a negative correlation between K^+ channel density and attenuation intensity.

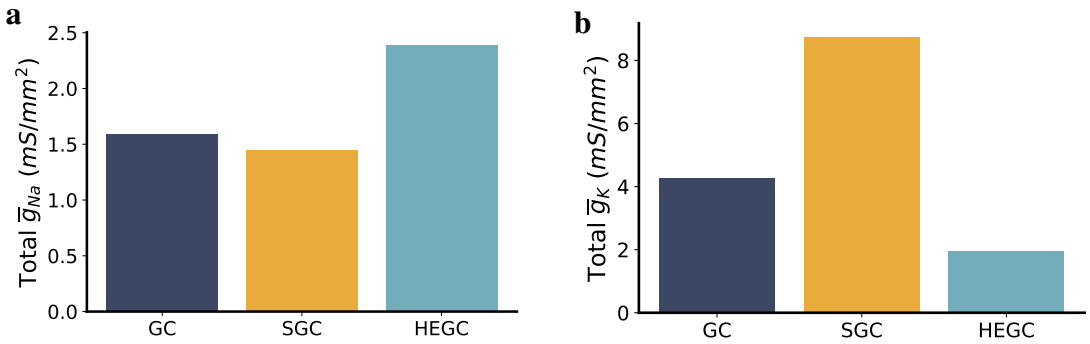

Figure 6. Total Na^+ and K^+ channel density in three types of granule cells. The density of ion channels in dendrites is represented by the value of maximum conductivity in the relevant dynamic equation. a) The $\overline{g}_{Na}$ in the entire dendritic branches of GCs, SGCs, and HEGCs was statistically analyzed, and b) $\overline{g}_{K}$ was also statistically analyzed. GCs: dark blue; SGCs: yellow; HEGCs: light blue.

3.4. Influence of morphology on the attenuation of backpropagating action potential

Dendritic structural complexity governed backpropagation efficacy through two synergistic mechanisms: branch order and diameter-dependent impedance modulation [12, 29]. The branch order, which reflected topological complexity while concurrently determining the velocity of action potential propagation, was classified using established morphological criteria [30]. Primary dendrites extending from the soma were designated as first-order branches. Subsequent bifurcations produced higher-order dendritic segments, which were further categorized into low-order dendrites (orders 1–3, colored blue) and high-order dendrites (orders > 4, colored pink, Figure 7a–c). Low-order dendrites predominated in SGCs (75.8%) compared to HEGCs (41.2%) and GCs (21.2%), creating parallel conductive pathways that amplified cumulative shunt currents (Figure 7d).

To evaluate potential contributions from dendritic dimensions, we further performed comparative dendritic segment length analysis (Figure 7e). Although HEGCs exhibited the longest low-order dendritic segments (median: Q_2 = 83.65 μm) and the shortest high-order dendritic segments (Q_2 = 48.27 μm), no significant correlation was found between dendritic segment length and attenuation intensity across different branch orders. In summary, integrating our findings on the attenuation amplitude order (SGC: 1.15 > HEGC: 0.8218 > GC: 0.3214) and the proportion of low-order

dendrites (SGC > HEGC > GC), we conclude that dendrite morphology with a higher proportion of low-order dendrites generates a unique electrical tension structure, facilitating axial current shunting through parallel conduction paths, leading to greater attenuation amplitude.

Furthermore, the diameter determines the propagation speed of the action potential. Sudden changes in the diameter between branches (referring to parent dendrites and daughter dendrites) can lead to transient changes in the action potential, such as propagation delay and so on. Therefore, the geometric ratio (GR), used to measure the complexity of the dendritic morphology, clarifies how it affects the propagation efficiency of the action potential. Subsequently, we computed GR for the three types of GCs, with detailed calculation methods mentioned by Goldstein and Acker [31, 32]. Selecting the longest dendrite on each type of GC. The longest dendrite of each type of GC was chosen as the main dendrite, and the GR was calculated along it at each branch point using the formula (3.1). The equation for calculating the GR is as follows [33]:

$$\mathrm{GR} = \frac{\sum_j d_j^{3/2}}{d_p^{3/2}}. \tag{3.1}$$

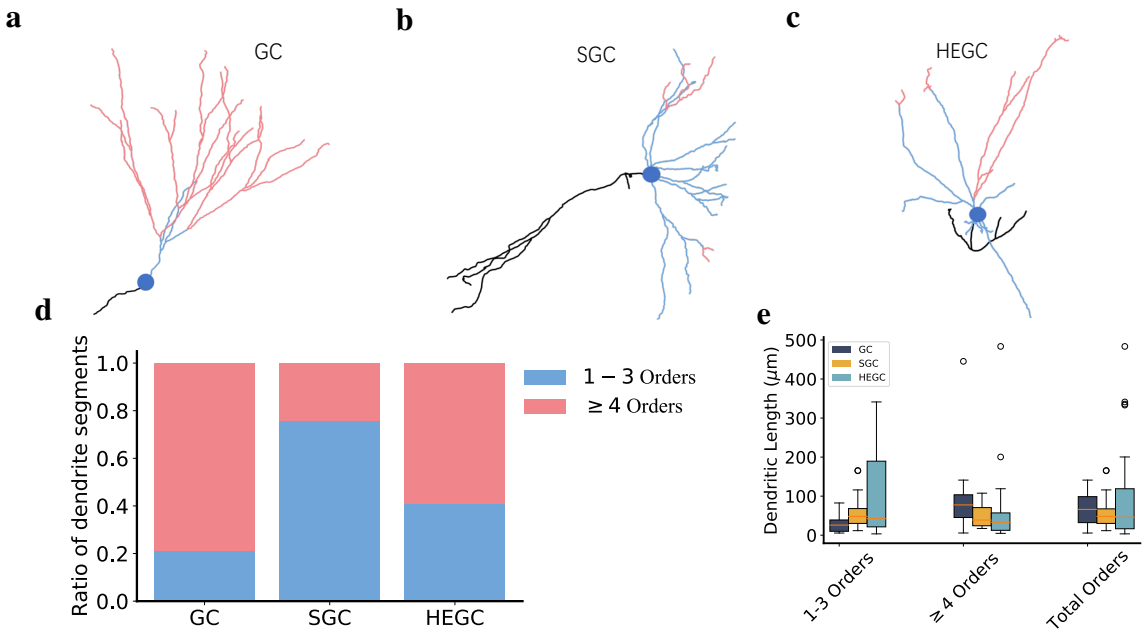

Figure 7. The dendritic branch order of three types of granule cells. The low-order and high-order dendritic branches are marked in the morphologies of a) GCs, b) SGCs, and c) HEGCs. Low-order branches are indicated in blue, while high-order branches are indicated in pink. The location of the soma is marked in dark blue. d) The proportion of low-order and high-order branches relative to the total number of dendrites is presented. e) Statistical analysis of branch lengths for different orders of dendrites (GCs: dark blue, SGCs: yellow, HEGCs: light blue) is provided.

Here, d_j and d_p represent the diameters of the daughter and parent branches, respectively. Specifically, when the GR is greater than 1, the resulting impedance mismatch induces the reflection

of axial currents back towards the soma, thus reducing the amplitude of the propagating wave. On the contrary, when GR is less than 1, diameter expansions enhance impedance matching, enabling more efficient transfer of current to the distal dendrites. Precisely when GR equals 1, the branch point maintains perfect impedance continuity, and the action potential amplitude is preserved during propagation.

As depicted in Figure 8, the value of GR along the main dendrite at each branch point in three types of granule cells was as follows. The GR of GCs at various branch points is approximately around 1.5; SGCs had elevated values in the range of 2.0–2.5; and HEGCs maintained uniform values of 2.0. The hierarchy of GR standard deviations (SGC: 2.15 ± 0.3 > HEGC: 1.85 ± 0.2 > GC: 1.44 ± 0.2) directly corresponds to the attenuation amplitude measurements (SGC: 1.15 > HEGC: 1.08 > GC: 0.94), which demonstrates the dominant role of morphology in signal regulation.

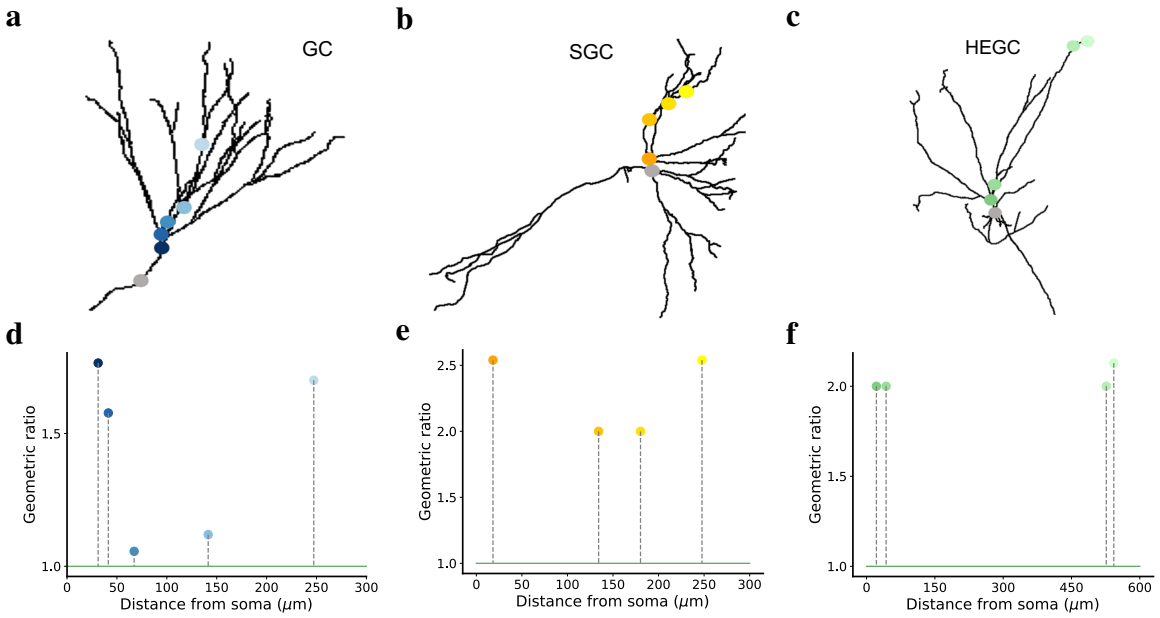

Figure 8. The dendritic geometric ratios of three types of granule cells. a–c) For GCs, SGCs, and HEGCs, the positions of the branch points utilized to calculate the geometric ratios in the main dendritic branch are marked with blue dots, yellow dots, and green dots, respectively, while the location of the soma is marked with gray dots. d–f) The dots stand for the geometric ratios computed for each branch point along the main dendrite of GCs (blue dots), SGCs (yellow dots), and HEGCs (green dots). The green line depicts the tendency of the geometric ratios along the main dendrites.

Collectively, these findings show that dendritic morphology impacts attenuation metrics via two synergistic pathways. First, the proliferation of low-order dendrites augments axial current shunting through parallel conductive pathways. Second, impedance mismatches mediated by the GR at branch points promote retrograde current reflection. Although morphological parameters predominantly control the attenuation amplitude, a comprehensive understanding of attenuation dynamics calls for the integration of active membrane properties in order to fully explain subtype-specific functional variances.

4. Conclusions and discussion

Backpropagation of action potentials in dentate granule cells differs across cell types, reflecting their intrinsic biophysical properties. Our models showed a clear hierarchy of attenuation: SGCs had the strongest attenuation, with the largest amplitude reduction (1.15), the highest attenuation rate (0.0256), and the shortest propagation distance (45.78 μm). HEGCs had the weakest attenuation, with the lowest rate (0.0083) and the longest distance (124.64 μm), while GCs were in between.

These differences largely result from the interaction between each granule cell's biophysical properties and their morphologies. For passive properties, R_a mainly determines the spatial scale of signal decay, affecting propagation distance but having little effect on attenuation amplitude or rate. For active properties, higher Na^+ channel density mainly reduces the attenuation rate and increases propagation distance, while the effect on attenuation amplitude is minor. Higher K^+ channel density mainly increases the attenuation rate through stronger current shunting, with smaller effects on attenuation amplitude. Dendritic morphology also plays an important role. SGCs have two notable features: a higher proportion of low-order dendrites and a larger mean value of GR. Both relate to dendritic diameter and together increase local current loss, leading to higher attenuation amplitude. In short, attenuation amplitude is predominantly determined by the proportion of low-order dendrites and the mean value of GR, whereas attenuation rate is mainly shaped by dendritic Na^+ and K^+ channel distribution densities, and propagation distance is largely governed by R_a. These relationships are summarized in Table 1, highlighting the dominant contributions of passive properties, active properties, and morphology to the three metrics of attenuation.

Table 1. Electrophysiological and morphological factors influencing attenuation in dentate granule cells. ✓ indicates a strong influence, × indicates no or minimal influence.

Factors	Amplitude	Attenuation rate	Propagation distance
R_a	×	×	✓
R_m	×	×	×
C_m	×	×	×
g_{leak}	×	×	×
Na^+ channel density	×	✓	✓
K^+ channel density	×	✓	✓
Low-order dendritic proportion	✓	×	×
High-order dendritic proportion	×	×	×
Low-order dendritic length	×	×	×
High-order dendritic length	×	×	×
GR	✓	×	×

The functional implication of this attenuation was profound for dentate circuit operations. As

demonstrated by Krueppel et al. [20], strong attenuation in GCs promoted network sparsity, a fundamental requirement for pattern separation. In SGCs, pronounced attenuation enforced somatic-dendritic decoupling through enhanced current shunting, preventing dendritic spike generation and reducing neuronal excitability. This mechanism aligned with evidence that SGCs enhanced network sparsity through controlled dendritic integration [17, 34], consistent with their role in optimizing pattern separation [35]. Conversely, weak attenuation in HEGCs maintained high dendritic signal fidelity, facilitating dendritic spike initiation and increasing neuronal excitability. This biophysical property explained how HEGCs disrupted pattern separation through excessive network synchronization [23], consistent with their pathological role in epileptogenesis [36].

Moreover, these functional differences arise from intrinsic cellular properties. In SGCs, K^+-dependent inhibitory mechanisms, along with shunting inhibition, strongly shape their electrophysiological behavior [25, 37]. By contrast, HEGCs under epileptic conditions exhibit heightened intrinsic excitability, characterized by self-bursting [38, 39], largely due to upregulation of voltage-gated Na^+ channels that increase sodium currents and dendritic excitability [40]. Corroborating this, many studies have also demonstrated that Na^+ channels facilitate dendritic action potential propagation, whereas K^+ channels limit it [9, 41]. Concerning passive properties, high axial resistance restricts intracellular current flow, promoting signal attenuation [42, 43]. With respect to dendritic morphology, Tian et al. [12] showed that a higher proportion of low-order dendrites accelerates bpAPs' velocity in hippocampal neurons, while Acker et al. [32] found in rat neocortical pyramidal neurons that larger GR values enhance current shunting and increase attenuation.

Collectively, these findings indicate that intrinsic membrane properties and dendritic morphology together determine subtype-specific excitability and signal propagation in dentate granule cells. This framework explains how distinct cellular subtypes differently influence circuit computations and highlights that cellular intrinsic properties fundamentally shape network function.

5. Study limitations

Although our models shed light on how passive, active, and morphological factors influence attenuation of bpAPs, certain aspects remain outside the present work. In particular, the models did not incorporate dendritic spines or synaptic specializations. Yet in biological neurons, spines constitute the primary sites of excitatory input and contain voltage-gated conductances capable of shaping local depolarization and ion flow [44]. Variations in spine geometry and density alter the effective membrane surface area and local input resistance, thereby affecting both current shunting and backpropagation. Notably, pathological conditions often involve spine loss or enlargement, structural changes that can modify local electrical load and ultimately influence the amplitude of bpAPs reaching distal dendritic regions [45].

Of particular relevance are the structural changes observed in HEGCs. Unlike normotopic granule cells, HEGCs frequently form aberrant recurrent excitatory connections and exhibit a higher density of dendritic spines [46, 47]. Combining our previous findings, the increase in dendritic spines is predicted to further reduce attenuation intensity in HEGCs. Additionally, the extra spine load may redistribute charge and partially offset local shunting. Collectively, these mechanisms provide a plausible explanation for why HEGCs display weaker attenuation and longer propagation distances compared with normotopic granule cells, thereby promoting excessive dendritic excitability and

predisposing the network to pathological synchronization.

Future work should integrate high-resolution reconstructions of dendritic spines and synaptic distributions into the models. Combining such detailed morphologies with in vitro recordings would clarify how spine and synapses jointly alter backpropagation, particularly in the context of epileptogenesis.

Use of AI tools declaration

The authors declare they have not used Artificial Intelligence (AI) tools in the creation of this article.

Conflict of interest

The authors declare there is no conflict of interest.

Funding

This work was supported by the National Natural Science Foundation of China (grant number 12572065).

Data availability

Data supporting all figures is available from the corresponding author upon reasonable request.

Authors contribution

Y. M. and X. S. designed the study, conducted the research, analyzed data, and drafted the paper. Meanwhile, M. L. provided detailed guidance for both paper writing and program design. All authors consented to be responsible for the content of this work.

References

1. G. Stuart, N. Spruston, B. Sakmann, M. Häusser, Action potential initiation and backpropagation in neurons of the mammalian CNS, *Trends Neurosci.*, **20** (1997), 125–131. https://doi.org/10.1016/s0166-2236(96)10075-8
2. P. Vetter, A. Roth, M. Häusser, Propagation of action potentials in dendrites depends on dendritic morphology, *J. Neurophysiol.*, **85** (2001), 926–937. https://doi.org/10.1152/jn.2001.85.2.926
3. J. Brunner, J. Szabadics, Analogue modulation of back-propagating action potentials enables dendritic hybrid signalling, *Nat. Commun.*, **7** (2016), 13033. https://doi.org/10.1038/ncomms13033
4. N. L. Golding, W. L. Kath, N. Spruston, Dichotomy of action-potential backpropagation in CA1 pyramidal neuron dendrites, *J. Neurophysiol.*, **86** (2001), 2998–3010. https://doi.org/10.1152/jn.2001.86.6.2998

5. D. Johnston, J. C. Magee, C. M. Colbert, B. R. Christie, Active properties of neuronal dendrites, *Annu. Rev. Neurosci.*, **19** (1996), 165–186. https://doi.org/10.1146/annurev.ne.19.030196.001121

6. T. Bock, A. Negrean, S. A. Siegelbaum, Somatic depolarization enhances hippocampal CA1 dendritic spike propagation and distal input driven synaptic plasticity, *J. Neurosci.*, **42** (2022), 3406–3425. https://doi.org/10.1523/JNEUROSCI.0780-21.2022

7. C. Schmidt-Hieber, P. Jonas, J. Bischofberger, Subthreshold dendritic signal processing and coincidence detection in dentate gyrus granule cells, *J. Neurosci.*, **27** (2007), 8430–8441. https://doi.org/10.1523/jneurosci.1787-07.2007

8. M. Häusser, G. Stuart, C. Racca, B. Sakmann, Axonal initiation and active dendritic propagation of action potentials in substantia nigra neurons, *Neuron*, **15** (1995), 637–647. https://doi.org/10.1016/0896-6273(95)90152-3

9. J. Waters, A. Schaefer, B. Sakmann, Backpropagating action potentials in neurones: Measurement, mechanisms and potential functions, *Prog. Biophys. Mol. Biol.*, **87** (2005), 145–170. https://doi.org/10.1016/j.pbiomolbio.2004.06.009

10. O. Herreras, Propagating dendritic action potential mediates synaptic transmission in CA1 pyramidal cells in situ, *J. Neurophysiol.*, **64** (1990), 1429–1441. https://doi.org/10.1152/jn.1990.64.5.1429

11. R. W. Turner, L. Maler, T. Deerinck, S. R. Levinson, M. H. Ellisman, TTX-sensitive dendritic sodium channels underlie oscillatory discharge in a vertebrate sensory neuron, *J. Neurosci.*, **14** (1994), 6453–6471. https://doi.org/10.1523/jneurosci.14-11-06453.1994

12. W. Tian, L. Peng, M. Zhao, L. Tao, P. Zou, Y. Zhang, Dendritic morphology affects the velocity and amplitude of back-propagating action potentials, *Neurosci. Bull.*, **38** (2022), 1330–1346. https://doi.org/10.1007/s12264-022-00931-9

13. T. Hainmueller, M. Bartos, Dentate gyrus circuits for encoding, retrieval and discrimination of episodic memories, *Nat. Rev. Neurosci.*, **21** (2020), 153–168. https://doi.org/10.1038/s41583-019-0260-z

14. X. Zhang, P. Jonas, Integration of spatial and non-spatial information by heterogeneous dentate gyrus granule cells, *J. Life Sci.*, **2** (2020), 19–24.

15. A. Gupta, A. Proddutur, Y. J. Chang, V. Raturi, J. Guevarra, Y. Shah, et al., Dendritic morphology and inhibitory regulation distinguish dentate semilunar granule cells from granule cells through distinct stages of postnatal development, *Brain Struct. Funct.*, **225** (2020), 2841–2855. https://doi.org/10.1101/2019.12.17.880005

16. Y. Kasahara, H. Nakashima, K. Nakashima, Seizure-induced hilar ectopic granule cells in the adult dentate gyrus, *Front. Neurosci.*, **17** (2023), 1150283. https://doi.org/10.3389/fnins.2023.1150283

17. Y. Mao, M. Liu, X. Sun, Excitatory synaptic integration of three types of granule cells in the dentate gyrus, *Cognit. Neurodyn.*, **19** (2025), 40. https://doi.org/10.1007/s11571-025-10226-0

18. S. Chavlis, P. C. Petrantonakis, P. Poirazi, Dendrites of dentate gyrus granule cells contribute to pattern separation by controlling sparsity, *Hippocampus*, **27** (2017), 89–110. https://doi.org/10.1002/hipo.22675

19. S. Kim, Y. Kim, S. H. Lee, W. K. Ho, Dendritic spikes in hippocampal granule cells are necessary for long-term potentiation at the perforant path synapse, *eLife*, **7** (2018), e35269. https://doi.org/10.7554/eLife.35269

20. R. Krueppel, S. Remy, H. Beck, Dendritic integration in hippocampal dentate granule cells, *Neuron*, **71** (2011), 512–528. https://doi.org/10.1016/j.neuron.2011.05.043

21. M. Häusser, B. Mel, Dendrites: Bug or feature, *Curr. Opin. Neurobiol.*, **13** (2003), 372–383. https://doi.org/10.1016/s0959-4388(03)00075-8

22. P. Jedlicka, L. Benuskova, W. C. Abraham, A voltage-based STDP rule combined with fast BCM-like metaplasticity accounts for LTP and concurrent "heterosynaptic" LTD in the dentate gyrus in vivo, *PLoS Comput. Biol.*, **11** (2015), e1004588. https://doi.org/10.1371/journal.pcbi.1004588

23. H. Yin, X. Sun, K. Yang, Y. Lan, Z. Lu, Regulation of dentate gyrus pattern separation by hilus ectopic granule cells, *Cognit. Neurodyn.*, **19** (2025), 10. https://doi.org/10.1007/s11571-024-10204-y

24. M. L. Hines, N. T. Carnevale, NEURON: A tool for neuroscientists, *Neuroscientist*, **7** (2001), 123–135. https://doi.org/10.1177/107385840100700207

25. K. R. Kim, S. Y. Lee, S. H. Yoon, Y. Kim, H. J. Jeong, S. Lee, et al., Kv4.1, a key ion channel for low frequency firing of dentate granule cells, is crucial for pattern separation, *J. Neurosci.*, **40** (2020), 2200–2214. https://doi.org/10.1523/JNEUROSCI.1541-19.2020

26. N. L. Golding, T. J. Mickus, Y. Katz, W. L. Kath, N. Spruston, Factors mediating powerful voltage attenuation along CA1 pyramidal neuron dendrites, *J. Physiol.*, **568** (2005), 69–82. https://doi.org/10.1113/jphysiol.2005.086793

27. J. H. Goldberg, G. Tamas, R. Yuste, Ca^{2+} imaging of mouse neocortical interneurone dendrites: I_a-type K^+ channels control action potential backpropagation, *J. Physiol.*, **551** (2003), 49–65. https://doi.org/10.1113/jphysiol.2003.042580

28. H. Y. Jung, T. Mickus, N. Spruston, Prolonged sodium channel inactivation contributes to dendritic action potential attenuation in hippocampal pyramidal neurons, *J. Neurosci.*, **17** (1997), 6639–6646. https://doi.org/10.1523/JNEUROSCI.17-17-06639.1997

29. Z. He, S. Zhang, Q. Song, W. Li, D. Liu, H. Li, et al., The structural development of primary cultured hippocampal neurons on a graphene substrate, *Colloids Surf. B Biointerfaces*, **146** (2016), 442–451. https://doi.org/10.1016/j.colsurfb.2016.06.045

30. M. Diamantaki, M. Frey, P. Berens, P. Preston-Ferrer, A. Burgalossi, Sparse activity of identified dentate granule cells during spatial exploration, *eLife*, **5** (2016), e20252. https://doi.org/10.7554/elife.20252

31. S. S. Goldstein, W. Rall, Changes of action potential shape and velocity for changing core conductor geometry, *Biophys. J.*, **14** (1974), 731–757. https://doi.org/10.1016/s0006-3495(74)85947-3

32. C. D. Acker, J. A. White, Roles of IA and morphology in action potential propagation in CA1 pyramidal cell dendrites, *J. Comput. Neurosci.*, **23** (2007), 201–216. https://doi.org/10.1007/s10827-007-0028-8

33. W. Rall, Branching dendritic trees and motoneuron membrane resistivity, *Exp. Neurol.*, **1** (1959), 491–527. https://doi.org/10.1016/0014-4886(59)90046-9

34. V. Volman, H. Levine, T. J. Sejnowski, Shunting inhibition controls the gain modulation mediated by asynchronous neurotransmitter release in early development, *PLoS Comput. Biol.*, **6** (2010), e1000973. https://doi.org/10.1371/journal.pcbi.1000973

35. K. Yang, X. Sun, S. Zhu, The heterogeneous population of granule cells contributes to pattern separation of the dentate gyrus neural network, *Nonlinear Dyn.*, **112** (2024), 13465–13481. https://doi.org/10.1007/s11071-024-09730-5

36. M. Y. Yim, A. Hanuschkin, J. Wolfart, Intrinsic rescaling of granule cells restores pattern separation ability of a dentate gyrus network model during epileptic hyperexcitability, *Hippocampus*, **25** (2015), 297–308. https://doi.org/10.1002/hipo.22373

37. L. Dovek, K. Marrero, E. Zagha, V. Santhakumar, Cellular and circuit features distinguish dentate gyrus semilunar granule cells and granule cells activated during contextual memory formation, *eLife*, **14** (2025), e101428. https://doi.org/10.1101/2024.08.21.608983

38. R. Z. Zhan, J. V. Nadler, Enhanced tonic GABA current in normotopic and hilar ectopic dentate granule cells after pilocarpine-induced status epilepticus, *J. Neurophysiol.*, **102** (2009), 670–681. https://doi.org/10.1152/jn.00147.2009

39. M. C. Cameron, R. Zhan, J. V. Nadler, Morphologic integration of hilar ectopic granule cells into dentate gyrus circuitry in the pilocarpine model of temporal lobe epilepsy, *J. Comp. Neurol.*, **519** (2011), 2175–2192. https://doi.org/10.1002/cne.22623

40. J. N. Wood, J. P. Boorman, K. Okuse, M. D. Baker, Voltage-gated sodium channels and pain pathways, *J. Neurobiol.*, **61** (2004), 55–71. https://doi.org/10.1002/neu.20094

41. D. Johnston, D. A. Hoffman, J. C. Magee, N. P. Poolos, S. Watanabe, C. M. Colbert, et al., Dendritic potassium channels in hippocampal pyramidal neurons, *J. Physiol.*, **525** (2000), 75–81. https://doi.org/10.1111/j.1469-7793.2000.00075.x

42. A. J. Hudspeth, M. M. Poo, A. E. Stuart, Passive signal propagation and membrane properties in median photoreceptors of the giant barnacle, *J. Physiol.*, **272** (1977), 25–43. https://doi.org/10.1113/jphysiol.1977.sp012032

43. P. Alcami, A. El Hady, Axonal computations, *Front. Cell Neurosci.*, **13** (2019), 413. https://doi.org/10.3389/fncel.2019.00413

44. N. Spruston, Pyramidal neurons: Dendritic structure and synaptic integration, *Nat. Rev. Neurosci.*, **9** (2008), 206–221. https://doi.org/10.1038/nrn2286

45. J. Tønnesen, G. Katona, B. Rózsa, U. V. Nägerl, Spine neck plasticity regulates compartmentalization of synapses, *Nat. Neurosci.*, **17** (2014), 678–685. https://doi.org/10.1038/nn.3682

46. A. L. Althaus, S. J. Moore, H. Zhang, X. Du, G. G. Murphy, J. M. Parent, Altered synaptic drive onto birthdated dentate granule cells in experimental temporal lobe epilepsy, *J. Neurosci.*, **39** (2019), 7604–7614. https://doi.org/10.1523/JNEUROSCI.0654-18.2019

47. S. C. Danzer, Adult neurogenesis in the development of epilepsy, *Epilepsy Curr.*, **19** (2019), 316–320. https://doi.org/10.1177/1535759719868186

AIMS Press